Zhao *et al. Microstructures* 2023;3:2023022
DOI: 10.20517/microstructures.2022.46

Microstructures

Research Article

Open Access

Check for updates

Low-pressure-driven barocaloric effects at colinear-to-triangular antiferromagnetic transitions in $Mn_{3-x}Pt_{1+x}$

Xueting Zhao[1,2], Kun Zhang[1,2], Ji Qi[1,2], Peng Liu[1,2], Zhao Zhang[1,2], Lin Qu[1,2], Zhidong Zhang[1,2], Bing Li[1,2]

[1]Shenyang National Laboratory for Materials Science, Institute of Metal Research, Chinese Academy of Sciences, Shenyang 110016, Liaoning, China.
[2]School of Materials Science and Engineering, University of Science and Technology of China, Shenyang 110016, Liaoning, China.

Correspondence to: Prof. Bing Li, Shenyang National Laboratory for Materials Science, Institute of Metal Research, Chinese Academy of Sciences, 72 Wenhua Road, Shenyang 110016, Liaoning, China. E-mail: bingli@imr.ac.cn; Prof. Kun Zhang, Shenyang National Laboratory for Materials Science, Institute of Metal Research, Chinese Academy of Sciences, 72 Wenhua Road, Shenyang 110016, Liaoning, China. E-mail: kzhang@imr.ac.cn

How to cite this article: Zhao X, Zhang K, Qi J, Liu P, Zhang Z, Qu L, Zhang Z, Li B. Low-pressure-driven barocaloric effects at colinear-to-triangular antiferromagnetic transitions in $Mn_{3-x}Pt_{1+x}$. *Microstructures* 2023;3:2023022. https://dx.doi.org/10.20517/microstructures.2022.46

Received: 29 Dec 2022 **First Decision:** 31 Jan 2023 **Revised:** 23 Mar 2023 **Accepted:** 21 Apr 2023 **Published:** 28 Apr 2023

Academic Editor: Fei Li **Copy Editor:** Fangling Lan **Production Editor:** Fangling Lan

Abstract

A large driving pressure is required for barocaloric effects (BCEs) in intermetallics, usually above 100 MPa. Here, we report barocaloric effects in $Mn_{3-x}Pt_{1+x}$ alloys saturated at about 60 MPa, the lowest pressure reported in intermetallics to date. A first-order phase transition occurs from the colinear antiferromagnetic phase to the triangular antiferromagnetic phase as temperature decreases. The transition temperature strongly depends on the composition x, ranging from 331 K for x = 0.18 to 384 K for x = 0.04, and is sensitive to pressure, with dT_t/dP up to 139 K/GPa. However, the maximum pressure-induced entropy changes are as small as 13.79 J kg^{-1} K^{-1}, attributed to the mutual cancellation of lattice and magnetic entropy changes. The small driving pressure and total entropy changes are due to the special magnetic geometric frustration.

Keywords: Barocaloric effects, magnetoelastic coupling, magnetic transition, geometrical spin frustration, colinear antiferromagnetic

INTRODUCTION

Refrigeration technology is of great significance for both industry and everyday life. Current refrigeration systems are mostly based on conventional vapor compression technology. Although highly optimized in recent decades, they still have a considerable undesirable impact on the environment[1]. Frequently used refrigerants have thousand-time stronger global warming potentials compared to CO_2. To achieve carbon neutrality, solid-state refrigeration technology based on the caloric effects of solids has been proposed as an alternative solution. Various phase transitions caused by some calorimeter materials under external fields are accompanied by huge latent heat, which can be utilized for cooling purposes through designated thermodynamic cycles. Magnetocaloric effects (MCEs) is one of the most studied caloric effects, which is usually linked to magnetic-field-induced first-order transitions. Barocaloric effects (BCEs), as the counterpart and extension of the (MCEs), is defined as the change in the isothermal entropy or adiabatic temperature of the material during the application or withdrawal of the external pressure field. Materials with first-order phase transition are more likely to be the most potential barocaloric effect materials due to the sensitivity of the lattice to pressure.

Initially observed around 2,000 years, BCEs has been found in $Pr_{1-x}La_xNiO_3$[2] and CeSb[3]. Subsequent studies of magneto-elastically coupled materials for MCEs have revealed larger BCEs, such as in magnetic shape memory alloys including NiMnIn[4], $La(Fe,Si)_{13}$[5,6], $Gd_5Si_2Ge_2$[7], $MnCoGe_{0.99}In_{0.01}$[8], FeRh[9,10], and others. These materials exhibit a strong coupling between magnetic and lattice degrees of freedom. Usually, there is a magnetic phase with a larger volume and a magnetic phase with a smaller volume. The application of a sufficiently large hydrostatic pressure induces a change of the system from the large-volume to the small-volume phase, and simultaneously the magnetic phase transition takes place. Typically, the required driving pressures in these systems are as high as several hundred MPa, and a comparable pressure-induced entropy change to that induced by a magnetic field can be obtained.

In recent years, a great variety of materials have been reported with larger BCEs, such as AgI[11], organic-inorganic hybrid chalcogenide $[TPrA][Mn(dca)_3]$[12], ferroelectric $(NH_4)_2SO_4$[13,14], spin-crossover complexes[15-18], and even natural rubber[19,20]. First-principles calculations also predicted sizable BCEs for lithium-ion conductor materials[21], fluorine ion conductor materials[22], and graphene[23]. In plastic crystals, the extensive molecular orientation disorder in plastic crystals leads to huge entropy changes larger than 100 J kg^{-1} K^{-1}, and the driving pressures have been significantly reduced down to below 100 MPa, for which they are termed as colossal barocaloric effects[24-26].

Antiferromagnetic materials are effective in releasing their entropy change by pressure in addition to the magnetic field[10,27], with remarkably reduced driving pressures, especially in frustrated antiferromagnets. Recent research has found that larger BCEs are observed at phase transitions from frustrated antiferromagnetic (AFM) to paramagnetic states in nitrides (Mn_3GaN[28], Mn_3NiN[29]) with an anti-perovskite structure. This indicates that even small hydrostatic pressures (as low as 90 MPa in plastic crystals) can effectively act on the AFM system. In this work, we report on the barocaloric properties of $Mn_{3-x}Pt_{1+x}$ alloys at first-order phase transitions from low-temperature triangle-lattice frustrated to high-temperature colinear AFM states. The composition-dependent phase transition temperature (T_t) is about 331 K for the $Mn_{2.82}Pt_{1.18}$. The pressure-dependent calorimetric measurements suggest that entropy changes are saturated at around 60 MPa.

EXPERIMENTS

Polycrystalline samples of $Mn_{3-x}Pt_{1+x}$ with different Mn contents (x = 0.04, 0.08, 0.1, and 0.18) were prepared by arc-melting the high-purity (99.9%) elements under an Ar atmosphere. The true composition was

determined using a ThermoFisher iCAP6300 Inductive Coupled Plasma Emission Spectrometer (ICP). The ingots were remelted three times to ensure homogeneity. 2wt.% excessive Mn elements were added to compensate for losses during the melting process. The as-prepared ingots were annealed in encapsulated quartz tubes at 973 K for 120 h and followed by furnace cooling. The nature of the single-phase was checked using a Rigaku MiniFlex 600 X-ray diffractometer. The temperature-dependent X-ray diffraction (XRD) patterns were collected using Bruker D8 Advance X-ray diffractometer. The diffraction patterns were fitted to a cubic unit cell (space group $Pm\bar{3}m$) in Jana2006[30]. The calorimetric data were collected as a function of temperature and pressure using a high-pressure differential scanning calorimeter (μDSC7, Setaram). The samples were enclosed in a high-pressure vessel made of Hastelloy. Constant pressure scans were performed at 0.1, 30, 60, and 90 MPa in the temperature region from 290 to 390 K, respectively. After subtracting the baseline background, the heat flow data can be converted to entropy changes. The magnetic properties are characterized using a Magnetic Properties Measurement System (MPMS-XL, Quantum Design) and a Physical Property Measurement System (PPMS-14T, Quantum Design).

RESULTS AND DISCUSSIONS

$Mn_{3-x}Pt_{1+x}$ crystallizes in the ordered Cu_3Au-type structure[31,32], where Mn atoms are located on the face centers of the cubic lattice formed by Pt atoms, as shown in Figure 1A. The compound with the stoichiometric composition magnetically orders into a colinear AFM state at about T_t ~365 K (magnetic transition temperature of Mn_3Pt in the literature[32]), where a negligibly small tetragonal distortion is observed. As depicted, magnetic moments carried by Mn atoms are aligned along the *c*-axis, and the magnetic unit cell is constructed along the *c*-axis with doubled chemical unit cell. Note that the Mn atoms located on the *ab*-plane carry no ordered magnetic moment. The four Mn atoms form a square lattice, and the diagonal magnetic moments are parallel while the adjacent ones are anti-parallel. Spaced by the non-magnetic Mn atom, the magnetic moments of the two layers of the square lattices are antiferromagnetically coupled. As the temperature decreases below T_t, such a colinear AFM state transforms into a triangle-lattice AFM state, where magnetic moments are located on the (111) plane and point in the <211> direction, leading to a two-dimensional geometric spin frustration. This arrangement of magnetic moments ensures that the magnetic unit cell is identical to the chemical unit cell. This phase transition is a typical first-order magnetic phase transition, even if the lattice symmetry is maintained[33]. Based on the triangular AFM structure, anomalous Hall effects have been predicted and observed in films as well as bulk single crystals[34,35].

In the $Mn_{3-x}Pt_{1+x}$ system, the magnetic properties, in particular, T_t, are strongly dependent on the composition *x*. Shown in Figure 1B is the heat flow data of the $x = 0.1$ alloy under ambient pressure, where an endothermic peak is found at 360 K while an exothermic peak at 340 K with a thermal hysteresis of about 20 K, which is a signature of the first-order phase transition. The temperature corresponding to the peak in the heat flow curve is defined as the phase transition temperature. In this paper, we uniformly regard the transition temperature of the cooling process as the phase transition temperature of the sample. The entropy change at this transition is derived from being about 12.31 J kg^{-1} K^{-1}, which is kind of small compared to other systems that exhibit strong first-order transitions. The reason will be clarified afterward. For example, the entropy change is 22.3 J kg^{-1} K^{-1} in Mn_3GaN[28] while 43 J kg^{-1} K^{-1} in Mn_3NiN[29]. The temperature-dependent XRD was used to monitor the lattice distortion during the phase transition. The contour plots of the XRD patterns are shown in Figure 1C as a function of temperature (*T*) and scattering vector (*Q*). The patterns can be indexed based on the reported cubic structure. Within our resolution, there is no distinguishable symmetry change in the temperature from 300 to 410 K. Four strong Bragg peaks are observed, and the (210) peak obviously shifts towards the lower *Q* around 360 K. The determined lattice constant displays a sudden jump at 360 K [Figure 1D], corresponding to relative changes in lattice constant

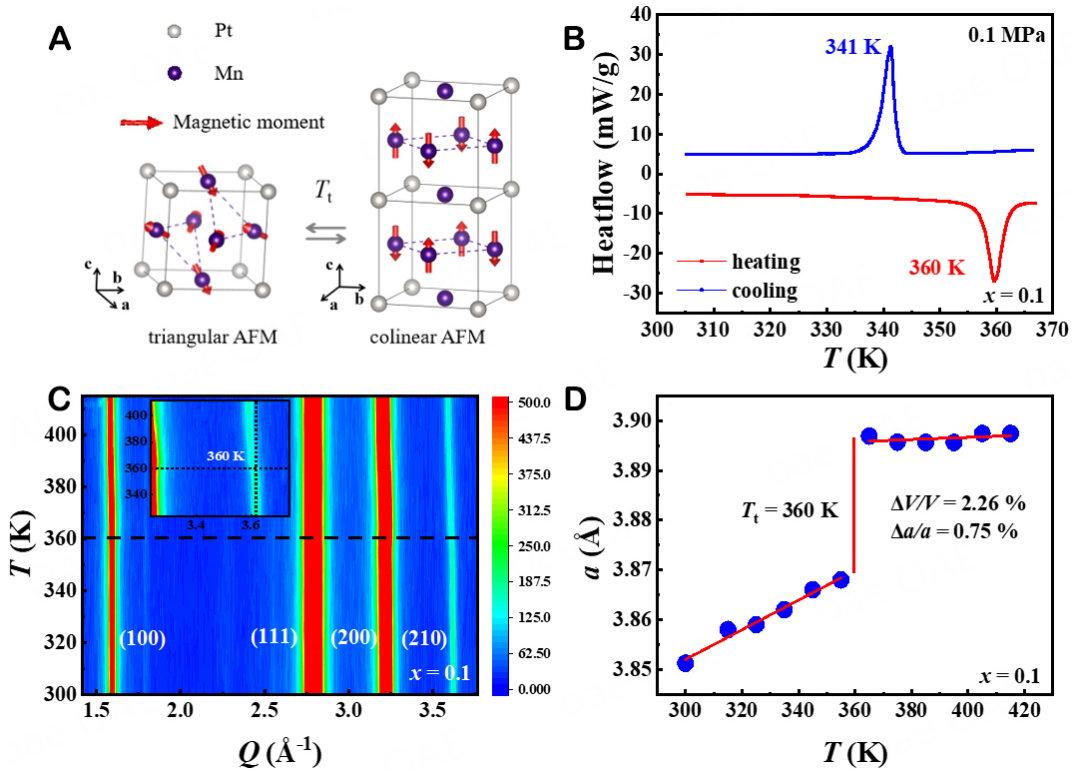

Figure 1. (A) Magnetic structures of Mn_3Pt alloys with triangular AFM and colinear AFM phases as reported by Tao *et al.*[27]. (B-D) heat flow *vs.* temperature curves, the contour plots of the variable temperature XRD patterns and lattice constant *vs.* temperature curves for sample x = 0.1, respectively. The inset in (C) is an enlarged image of the high Q region.

and unit cell volume of 0.75% and 2.26%, respectively. These values are similar to those reported in other literature[36,37]. In addition, the structurally determined T_t is well consistent with the thermally determined one.

After confirming the first-order phase transition as the core of this study typically occurs at x = 0.1, we systematically extend the magnetic characterizations to x = 0.04, 0.08, 0.1, and 0.18. Their field-cooled magnetizations as a function of temperature are plotted in Figure 2A-D. As the temperature decreases, magnetizations abruptly drop at 331 K for x = 0.18, 336 K for x = 0.1, 355 K for x = 0.08, and 384 K for x = 0.04, indicating the first-order phase transitions. As for x = 0.1, the determined T_t at the magnetization is a few kelvins lower than that in the heat flow data. We summarize the T_t values of these four samples, along with their lattice constants at room temperature, in Figure 2E. As x changes from 0.18 to 0.04, T_t monotonically increases while the lattice constant a decrease. Unlike the linear behavior of a, T_t exhibits a saturation feature, remaining nearly constant when x is greater than 0.1. Such a tendency is consistent with the previous report[31,32,36]. This phenomenon is also explained in the literature[31] based on the theoretical phase diagram of Mn_3Pt in the molecular field approximation.

Selecting x = 0.18 as an example, the high-field isothermal magnetization is considered at 300 and 380 K, where the compound is in the triangular AFM and colinear AFM states, respectively. As shown in Figure 2F, the magnetizations essentially obey a linear relation as a function of applied fields up to 14 T, which reflects the dominating AFM interactions. However, the low-field regions (the inset of Figure 2F) show a weak nonlinearity at both temperatures, which might be attributed to the uncancelled moments due to the off-stoichiometry. In particular, there are small remanence and coercivity at 300 K. The exact origin is

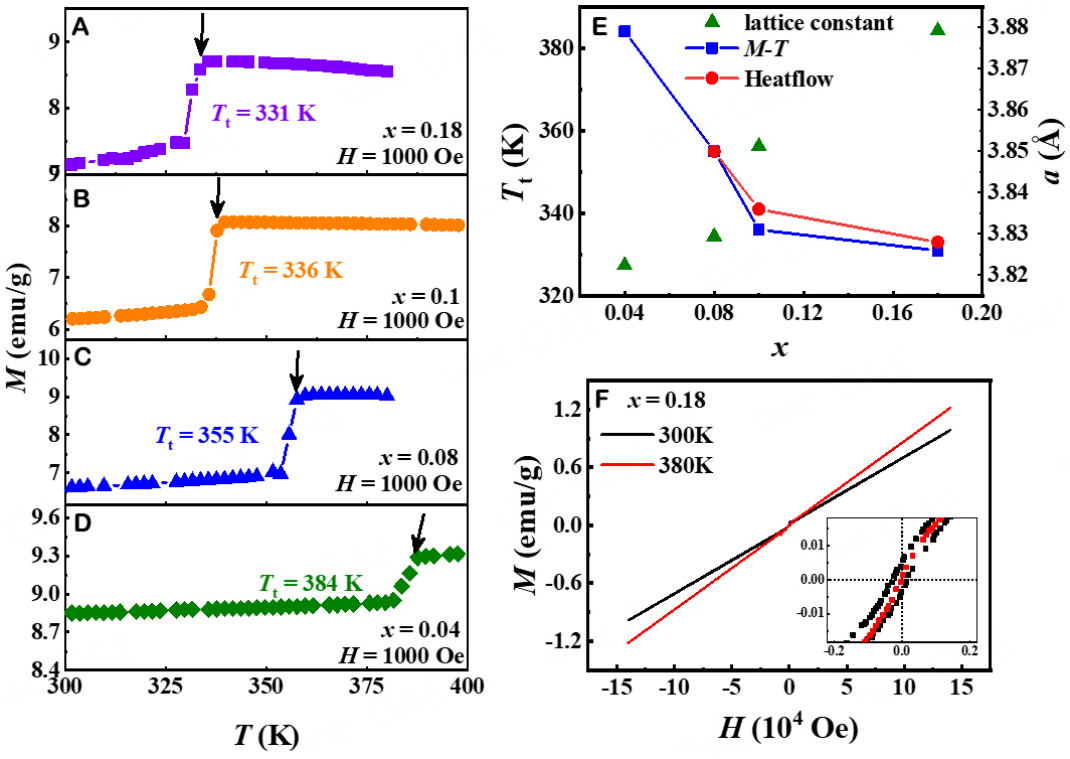

Figure 2. (A-D) Magnetization curves for samples x = 0.18, 0.1, 0.08, and 0.04, respectively. (E) Curves of phase transition temperature *vs.* manganese content x (blue squares and red dots indicate measurement by M-T and heat flow, respectively) and lattice constant *vs.* manganese content x for the samples. (Taking x = 0.08 as an example, the fitting parameters obtained using the lebail method to fit the XRD curve are: GOF = 1.47, Rp = 4.18, Rwp = 5.99). (F) The magnetization loop of x = 0.18. The inset shows the enlarged plot at low fields.

still unknown. Previous studies have also shown that a ferromagnetic component perpendicular to the (111) plane is allowed on both Mn and Pt atoms, except for the component in the (111) plane pointing in the [112] direction in the magnetic structure of the triangular AFM phase[31]. Furthermore, it has been pointed out that the origin of this ferromagnetism may be because the third site of the colinear AFM phase generates a net magnetic moment due to electron interactions at low temperatures of 100 K or even lower[38]. In contrast to the presence of net moments along the <111> direction, the magnetization curve of the single-crystal material along the <111> direction did not show ferromagnetic behavior[34].

Except for the influence of magnetic fields on the first-order phase transitions, we explore the impact of applied hydrostatic pressures. Heat flow data as a function of temperature are plotted under 0.1, 30, 60, and 90 MPa for x = 0.08 and x = 0.18 in Figure 3A and B, respectively. As the pressure increases, the endothermic and exothermic peaks move toward the high-temperature region simultaneously. The peak intensity has a small increase with pressure, while the peak width has a tendency to narrow, which is especially obvious in the x = 0.18 sample. In addition, the thermal hysteresis at 0.1 MPa for the x = 0.08 sample is the same as that at x = 0.1, which is 19 K. However, the thermal hysteresis at atmospheric pressure for x = 0.18 sample is 9 K and decreases to 5 K at 90 MPa with increasing pressure.

Entropy changes at the phase transition under constant pressure, ΔS_P, are determined by integrating the heat flow data. The pressure-induced entropy changes ($\Delta S_{P_0 \to P}$) when pressure is increased from ambient pressure (P_0) to applied pressure (P) is defined as $\Delta S_{P_0 \to P} = \Delta S_P - \Delta S_{P_0}$. Figure 3C and D show $\Delta S_{P_0 \to P}$ at the

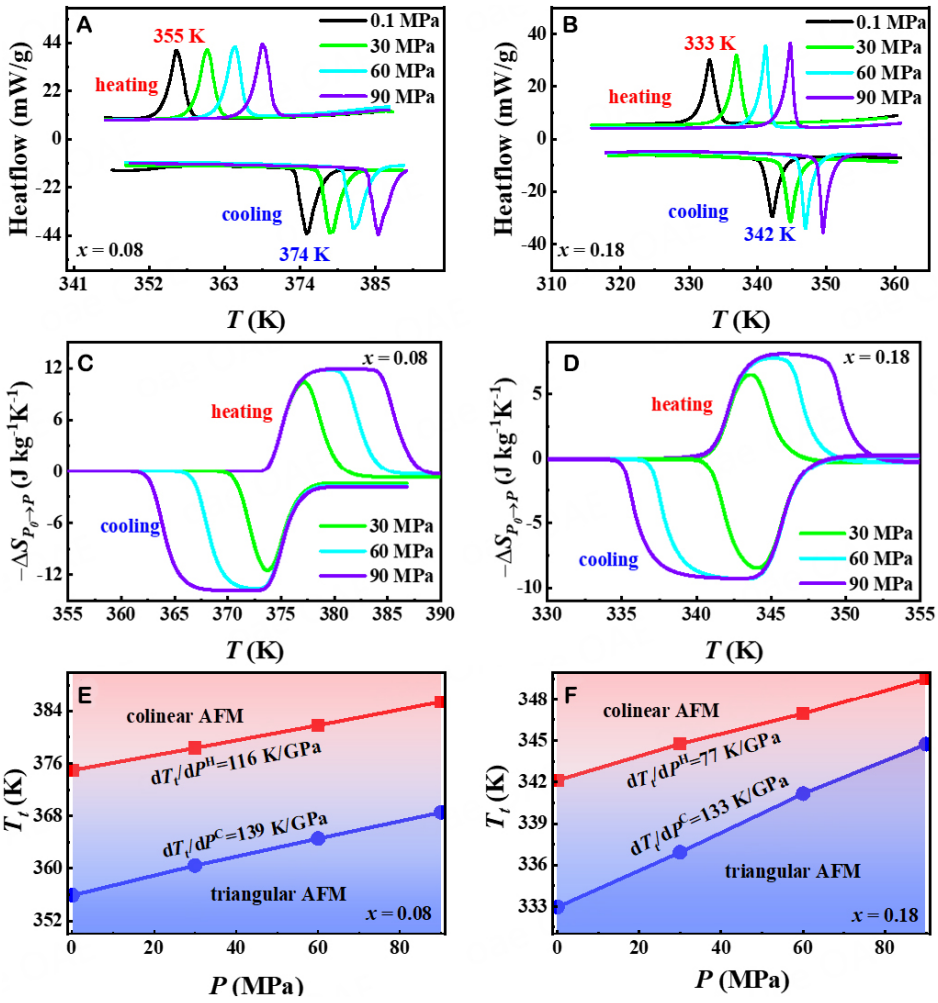

Figure 3. (A and B) Heat flow data as a function of temperature for x = 0.08 and x = 0.18 at 0.1, 30, 60, and 90 MPa pressure, respectively. (C and D) Entropy change curves for x = 0.08 and x = 0.18 at different pressures, respectively. (E and F) The temperature-pressure phase diagrams for x = 0.08 and x = 0.18, respectively.

final pressure of 30, 60, and 90 MPa for x = 0.08 and 0.18, respectively. It can be seen that more than 80% of the maximum entropy changes are achieved at pressures as low as 30 MPa, and the entropy changes tend to be saturated at about 60 MPa. Note that the maximum entropy of 13.79 J kg^{-1} K^{-1} acquired in x = 0.08 at 90 MPa is larger than that in x = 0.18 whereas the so-called reversible region (overlapped region for the cooling and heating curves) is much larger for x = 0.18. The temperature-pressure phase diagrams are constructed based on the heat flow data [Figure 3E and F]. It can be seen that the thermal hysteresis is much smaller in x = 0.18, which is the reason why its reversible region is larger[14]. Furthermore, its thermal hysteresis is obviously reduced at higher pressures.

To understand the uniqueness of this system, Table 1 compares its barocaloric factors to those of other typical compounds, including organic plastic crystals, inorganic salts, magnetocaloric intermetallics, and other frustrated AFM systems. The slope of the phase boundary (dT_t/dP) of this system is the largest, and the driving pressure (ΔP) is the smallest among all intermetallics, which are impressively comparable to those of prototype plastic crystal neopentyl glycol with colossal BCEs. However, the larger dT_t/dP must lead to smaller entropy changes in terms of the Clausius-Clapeyron relation[39], even though the volume change

Table 1. Performance summary of several typical barocaloric materials

Material	T_t (K)	dT_t/dP (K GPa^{-1})	P (MPa)	V/V (%)	$\Delta S_{P_0 \rightarrow P}$ (J kg^{-1}K^{-1})	Ref.
NPG	313	133	45	-	389	[24]
$C_2B_{10}H_{12}$	277	380	60	-	106.2	[44]
NH_4I	243	810	20	-	89	[45]
NH_4SCN	364	300	20	5	128.7	[46]
$Fe_{49}Rh_{51}$	310	60	250	1	12	[9,10]
$MnNiSi_{0.61}FeCoGe_{0.39}$	311	70	260	-	44	[47]
$Ni_{0.95}Fe_{0.05}S$	274	75	100	2	39.6	[48]
Mn_3GaN	290	65	90	1	21.6	[28]
Mn_3NiN	262	13.5	280	0.4	35	[29]
$Mn_{2.92}Pt_{1.08}$	355	139	60	2.26*	13.79	This work

*determined for $Mn_{2.9}Pt_{1.1}$.

is not too small. The small entropy change at this first-order phase transition is due to unique magnetic fluctuations in nature. Magnetic fluctuation refers to the fluctuation of magnetic (electron spin) moment in magnetic systems[40]. The interaction between the local moment and the itinerant electron matrix may enhance spin fluctuation. Frustration structures are often accompanied by strong spin fluctuations[41,42]. Neutron diffraction measurements suggest that the ordered moment is 3.3 μ_B/Mn atom in the colinear AFM state, whereas 2.2 μ_B/Mn atom in the triangular AFM[37]. The reduction in the latter should be attributed to spin fluctuations due to geometric frustration. As a result, the triangle-lattice AFM state is magnetically less ordered than the colinear AFM one, which leads to an increase of magnetic entropy across T_t. At the same time, the crystal lattice shows a normal contraction, and a reduction of entropy of the lattice subsystem is expected. We infer that the contributions of individuals to the total entropy change partially cancel each other out, and the remaining entropy change represents the overall entropy change of the material. According to the previous theoretic study, the system can be described by a nearest-neighboring exchange interaction J_1 and a next-nearest-neighboring exchange interaction J_2. J_1 is always negative, but J_2 can be negative or positive, dependent on the interatomic distance between Mn atoms[31]. At T_t, J_2 just changes its sign due to the shrinkage of the Mn-Mn distance. In this sense, such a picture is similar to the exchange striction observed in NiMnIn alloys[43].

CONCLUSIONS

In summary, the first-order phase transitions of $Mn_{3-x}Pt_{1+x}$ (x = 0.04, 0.08, 0.1, and 0.18) compounds have been studied at varying temperatures, pressures, and magnetic fields. At the phase transitions, both magnetizations and lattice constants showed abrupt drops as the temperature decreased. While the phase transition temperatures decreased at lower Mn content, they increased at higher pressures. This system is highly susceptible to pressure, and the pressure-induced entropy changes are saturated at 60 MPa, which is the lowest among current intermetallics. This may be due to the intense geometric magnetic frustration.

DECLARATIONS

Authors' contributions

Prepared the samples, collected the data, performed data analysis and contributed to the writing and revisions: Zhao X

Conceived the study, designed the study, and contributed to the writing and revisions: Li B, Zhang K

Collected some of the data and provided technical support: Qi J, Liu P, Zhang Z (Zhang Zhao), Qu L

Revision of articles: Zhang Z (Zhang Zhidong)

Availability of data and materials

The datasets used and analyzed during the current study are available from the corresponding author upon reasonable request.

Financial support and sponsorship

The work was supported by the Ministry of Science and Technology of China (Grant nos. 2021YFB3501201, 2022YFE0109900, and 2020YFA0406002) and the Key Research Program of Frontier Sciences of Chinese Academy of Sciences (Grant no. ZDBS-LY-JSC002).

Conflicts of interest

All authors declared that there are no conflicts of interest.

Ethical approval and consent to participate

Not applicable.

Consent for publication

Not applicable.

REFERENCES

1. Sari O, Balli M. From conventional to magnetic refrigerator technology. *Int J Refrig* 2014;37:8-15. DOI
2. Müller K, Fauth F, Fischer S, Koch M, Furrer A, Lacorre P. Cooling by adiabatic pressure application in $Pr_{1-x}La_xNiO_3$. *Appl Phys Lett* 1998;73:1056-8. DOI
3. Strässle T, Furrer A, Lacorre P, Müller K. A novel principle for cooling by adiabatic pressure application in rare-earth compounds. *J Alloys Compd* 2000;303-304:228-31. DOI
4. Mañosa L, González-Alonso D, Planes A, et al. Giant solid-state barocaloric effect in the Ni-Mn-In magnetic shape-memory alloy. *Nat Mater* 2010;9:478-81. DOI
5. Mañosa L, González-Alonso D, Planes A, et al. Inverse barocaloric effect in the giant magnetocaloric La-Fe-Si-Co compound. *Nat Commun* 2011;2:595. DOI
6. Fujieda S, Fujita A, Fukamichi K. Strong pressure effect on the curie temperature of itinerant-electron metamagnetic $La(Fe_{0.88}Si_{0.12})_{13}Hy$ and $La_{0.7}Ce_{0.3}(Fe_{0.88}Si_{0.12})_{13}Hy$. *Mater Trans* 2009;50:483-6. DOI
7. Yuce S, Barrio M, Emre B, et al. Barocaloric effect in the magnetocaloric prototype $Gd_5Si_2Ge_2$. *Appl Phys Lett* 2012;101:071906. DOI
8. Wu RR, Bao LF, Hu FX, et al. Giant barocaloric effect in hexagonal Ni_2In-type Mn-Co-Ge-In compounds around room temperature. *Sci Rep* 2015;5:18027. DOI PubMed PMC
9. Stern-taulats E, Gràcia-condal A, Planes A, et al. Reversible adiabatic temperature changes at the magnetocaloric and barocaloric effects in $Fe_{49}Rh_{51}$. *Appl Phys Lett* 2015;107:152409. DOI
10. Stern-taulats E, Planes A, Lloveras P, et al. Barocaloric and magnetocaloric effects in $Fe_{49}Rh_{51}$. *Phys Rev B* 2014;89:214105. DOI
11. Aznar A, Lloveras P, Romanini M, et al. Giant barocaloric effects over a wide temperature range in superionic conductor AgI. *Nat Commun* 2017;8:1851. DOI PubMed PMC
12. Bermúdez-García JM, Sánchez-Andújar M, Castro-García S, López-Beceiro J, Artiaga R, Señarís-Rodríguez MA. Giant barocaloric effect in the ferroic organic-inorganic hybrid $[TPrA][Mn(dca)_3]$ perovskite under easily accessible pressures. *Nat Commun* 2017;8:15715. DOI PubMed PMC
13. Lloveras P, Stern-Taulats E, Barrio M, et al. Giant barocaloric effects at low pressure in ferrielectric ammonium sulphate. *Nat Commun* 2015;6:8801. DOI PubMed PMC
14. Mikhaleva E, Gorev M, Bondarev V, Bogdanov E, Flerov I. Comparative analysis of elastocaloric and barocaloric effects in single-crystal and ceramic ferroelectric $(NH_4)_2SO_4$. *Scripta Mater* 2021;191:149-54. DOI
15. Yu C, Huang J, Qi J, et al. Giant barocaloric effects in formamidinium iodide. *APL Mater* 2022;10:011109. DOI
16. Salgado-beceiro J, Nonato A, Silva RX, et al. Near-room-temperature reversible giant barocaloric effects in $[(CH_3)_4N]Mn[N_3]_3$ hybrid perovskite. *Mater Adv* 2020;1:3167-70. DOI
17. Ranke P, Alho B, Ribeiro P. First indirect experimental evidence and theoretical discussion of giant refrigeration capacity through the

reversible pressure induced spin-crossover phase transition. *J Alloys Compd* 2018;749:556-60. DOI

18. Szafrański M, Wei W, Wang Z, Li W, Katrusiak A. Research update: tricritical point and large caloric effect in a hybrid organic-inorganic perovskite. *APL Mater* 2018;6:100701. DOI
19. Bom NM, Imamura W, Usuda EO, Paixão LS, Carvalho AMG. Giant barocaloric effects in natural rubber: a relevant step toward solid-state cooling. *ACS Macro Lett* 2018;7:31-6. DOI
20. Miliante CM, Christmann AM, Usuda EO, et al. Unveiling the origin of the giant barocaloric effect in natural rubber. *Macromolecules* 2020;53:2606-15. DOI
21. Sagotra AK, Chu D, Cazorla C. Room-temperature mechanocaloric effects in lithium-based superionic materials. *Nat Commun* 2018;9:3337. DOI PubMed PMC
22. Cazorla C, Errandonea D. Giant mechanocaloric effects in fluorite-structured superionic materials. *Nano Lett* 2016;16:3124-9. DOI PubMed
23. Ma N, Reis MS. Barocaloric effect on graphene. *Sci Rep* 2017;7:13257. DOI PubMed PMC
24. Li B, Kawakita Y, Ohira-Kawamura S, et al. Colossal barocaloric effects in plastic crystals. *Nature* 2019;567:506-10. DOI
25. Aznar A, Lloveras P, Barrio M, et al. Reversible and irreversible colossal barocaloric effects in plastic crystals. *J Mater Chem A* 2020;8:639-47. DOI
26. Lloveras P, Tamarit J. Advances and obstacles in pressure-driven solid-state cooling: a review of barocaloric materials. *MRS Energy Sustain* 2021:8;3-15. DOI
27. Tao K, Song W, Lin J, et al. Giant reversible barocaloric effect with low hysteresis in antiperovskite $PdNMn_3$ compound. *Scripta Mater* 2021;203:114049. DOI
28. Matsunami D, Fujita A, Takenaka K, Kano M. Giant barocaloric effect enhanced by the frustration of the antiferromagnetic phase in Mn_3GaN. *Nat Mater* 2015;14:73-8. DOI PubMed
29. Boldrin D, Mendive-tapia E, Zemen J, et al. Multisite exchange-enhanced barocaloric response in Mn_3NiN. *Phys Rev X* 2018;8:041035. DOI
30. Dusek M, Petricek V. Towards the routine application of computing system Jana2000. *Acta Crystallogr A Found Crystallogr* 2005;61:c104-5. DOI
31. Krén E, Kádár G, Pál L, Sólyom J, Szabó P, Tarnóczi T. Magnetic structures and exchange interactions in the Mn-Pt system. *Phys Rev* 1968;171:574-85. DOI
32. Krén E, Kádár G, Pál L, Szabó P. Investigation of the first-order magnetic transformation in Mn_3Pt. *J Appl Phys* 1967;38:1265-6. DOI
33. Tomiyoshi S, Yasui H, Kaneko T, et al. Magnetic excitations in Mn_3Pt at high energies by the TOF method. *J Magn Magn Mater* 1990;90-91:203-4. DOI
34. Zuniga-Cespedes BE, Manna K, Noad HML, et al. Observation of an anomalous hall effect in single-crystal Mn_3Pt. *Mater Sci* 2022;2209:05865. DOI
35. An N, Tang M, Hu S, et al. Structure and strain tunings of topological anomalous hall effect in cubic noncollinear antiferromagnet Mn_3Pt epitaxial films. *Sci China Phys Mech Astron* 2020;63:297511. DOI
36. Yasui H, Kaneko T, Yoshida H, Abe S, Kamigaki K, Mori N. Pressure dependence of magnetic transition temperatures and lattice parameter in an antiferromagnetic ordered alloy Mn_3Pt. *J Phys Soc Jpn* 1987;56:4532-9. DOI
37. Yasui H, Ohashi M, Abe S, et al. Magnetic order-order transformation in Mn_3Pt. *J Magn Magn Mater* 1992;104-107:927-8. DOI
38. Ricodeau JA. Model of the antiferromagnetic-antiferromagnetic transition in Mn_3Pt alloys. *J Phys F Met Phys* 1974;4:1285-303. DOI
39. Boldrin D. Fantastic barocalorics and where to find them. *Appl Phys Lett* 2021;118:170502. DOI
40. Ehrenreich H, Spaepen F. Solid state physics: advances in research and applications. Amsterdam Boston: Academic Press; 2006.
41. Hemberger J, von Nidda HA, Tsurkan V, Loidl A. Large magnetostriction and negative thermal expansion in the frustrated antiferromagnet $ZnCr_2Se_4$. *Phys Rev Lett* 2007;98:147203. DOI PubMed
42. Broholm C, Aeppli G, Espinosa GP, Cooper AS. Antiferromagnetic fluctuations and short-range order in a Kagomé lattice. *Phys Rev Lett* 1990;65:3173-6. DOI
43. Li B, Ren WJ, Zhang Q, et al. Magnetostructural coupling and magnetocaloric effect in Ni-Mn-In. *Appl Phys Lett* 2009;95:172506. DOI
44. Zhang K, Song R, Qi J, et al. Colossal barocaloric effect in carboranes as a performance tradeoff. *Adv Funct Mater* 2022;32:2112622. DOI
45. Ren Q, Qi J, Yu D, et al. Ultrasensitive barocaloric material for room-temperature solid-state refrigeration. *Nat Commun* 2022;13:2293. DOI PubMed PMC
46. Zhang Z, Li K, Lin S, et al. Thermal batteries based on inverse barocaloric effects. *Sci Adv* 2023;9:eadd0374. DOI PubMed PMC
47. Lloveras P, Samanta T, Barrio M, et al. Giant reversible barocaloric response of $MnNiSi)_{1-x}(FeCoGe)_x$ (x = 0.39, 0.40, 0.41). *APL Mater* 2019;7:061106. DOI
48. Greca LG, Lehtonen J, Tardy BL, Guo J, Rojas OJ. Biofabrication of multifunctional nanocellulosic 3D structures: a facile and customizable route. *Mater Horiz* 2018;5:408-15. DOI